IJP · CrossMark

ORIGINAL PAPER

Study of Ni:CeO$_2$ nanoparticles for efficient photodegradation of methylene blue by sun light irradiation

V Ramasamy*, V Mohana and G Suresh

Department of Physics, Annamalai University, Annamalai Nagar, Chidambaram 608 002, India

Abstract: Pure and different concentration of Ni-doped CeO$_2$ nanoparticles were synthesized using a sol–gel technique. The products were characterized by X-ray diffraction (XRD), UV–Vis absorption and photoluminescence (PL) spectroscopy, Fourier transform infrared spectroscopy (FTIR) and TG-DTA measurements. The XRD analysis dictated that the product has CeO$_2$ crystallites with cubic structure. The average crystallite size varied from 10.98 to 35.43 nm. The SEM-EDAX analysis shows the nature of morphology and the presence of elements. A suitable temperature is selected using TG-DTA analysis to tune the optical band gap. The HR-TEM pictures show that the particles are spherical in shape and affirmed the XRD investigation. The optical properties of the nanoparticles are seen by UV–visible and PL spectroscopy. The structural bond vibrations of pure and Ni-doped CeO$_2$ nanoparticles were analyzed by FTIR spectroscopy. The photocatalytic activity of pure and Ni-doped CeO$_2$ nanoparticles was assessed by methylene blue degradation in an aqueous solution which directed that the 0.1 M.% of the Ni-doped CeO$_2$ show the best photocatalytic movement.

1. Introduction

The photocatalysis, a technique which uses the visible radiation from sunlight and employs semiconductors such as photocatalysts, induces a chemical reaction to eliminate the organic pollutants present in dye wastewater [1]. Dye wastewater has attracted people's attention nowadays, since the synthetic dyes are widely used in various industries, such as textile, leather, paper and plastics. Due to their chemical stability and general toxicity, the dye pollutants are potentially harmful to the eco-environment when these pollutants are discharged to the rivers and lakes without any prior treatment. However, as dyes also absorb light, especially in the visible range, the influence of this photoabsorption by dyes should be excluded for evaluation of the real photocatalytic activity of photocatalysts [2]. Methylene blue is a cationic dye, used extensively for dying cotton, wool and silk. The risk of the presence of this dye in wastewater may arise from the burns effect of eye,

nausea, vomiting and diarrhoea [3]. In recent years, photocatalysis has been widely applied on the treatment of various wastewaters and resistant contaminants such as leather industry wastewater, dye wastewater, herbicides, heterocyclic compounds and others [4]. Many catalysts like TiO$_2$, ZnO, ZrO$_2$, WO$_3$, Fe$_2$O$_3$, CeO$_2$, CdS, ZnS and Pd/BiOI/MnOx have been attempted for the photocatalytic degradation of a wide variety of environmental contaminants [5, 6].

Cerium is a lanthanide series rare earth element and can exist in either the free metal or oxide form. It can cycle between the cerous, cerium (III), and ceric, cerium (IV) oxidation states [7]. Both oxidation states of cerium strongly absorb ultraviolet light and have two characteristic spectrophotometric absorbance peaks (230–260 and 300–400 nm) [8]. Over the past decade, cerium oxide nanoparticles have been widely studied for their structural, chemical, and physical properties. These particles have non-stoichiometry, reduction behaviour, oxygen storage capacity and interactions of metal/CeO$_2$ nanoparticles [9–11]. Cerium oxide (CeO$_2$) having cubic structure is the most important oxide due to its extraordinary chemical properties (acid-base and oxidation-reduction behaviour),

*Corresponding author, E-mail: srsaranram@rediffmail.com

thermal stability and oxygen mobility [12]. CeO_2 nanoparticles have shown many important applications such as fuel cells [13], catalyst [14], sunscreen cosmetics [15], sensor [16] and UV blockers [17]. Generally, CeO_2 nanoparticles were synthesized by physical and chemical methods [18–22]. Among these, the sol–gel method has become very popular due to its versatility, better purity, low processing temperature, and the possibility of controlling the size and morphology of grains [23].

In the present work, pure and Ni-doped CeO_2 nanoparticles were synthesized by sol–gel method. The nanoparticles were characterized by thermogravimetric and differential thermal analysis (TG-DTA), Ultraviolet–Visible spectroscopy (UV–Vis), X-ray diffraction (XRD), Scanning electron microscopy and energy dispersive X-ray analysis (SEM-EDX), High resolution transmission electron microscopy (HR-TEM), photoluminescence (PL) and Fourier transform infrared (FTIR) techniques. The photocatalytic activities were also studied under irradiation of sunlight.

2. Experimental details

2.1. Materials

The materials such as Cerium (IV) nitrate $[(NH_4)_2[Ce(NO_3)_6]$ from Nice Chemical company, Nickel acetate extra pure (Tetrahydrate) $(CH_3.COO)_2Ni·4H_2O$ from Loba Chemie PVT. LTD. Ammonium hydroxide (NH_3) from spectrum reagents and Chemicals Pvt. Ltd, Citric acid anhydrous $(C_6H_8O_7)$ from s–d Fine Chem. Ltd, and deionized water (DI) were used to synthesize pure and Ni-doped CeO_2 nanoparticles. All the chemicals were above 99% purity. For all dilution and sample preparation, ultrapure water was used. The glass wares used in work were acid washed.

2.2. Methods

Using sol–gel procedure, pure and Ni-doped CeO_2 nanoparticles were synthesized. In this experimental procedure, 5.2 g (0.4 M) of Cerium (IV) nitrate $(NH_4)_2[Ce(NO_3)_6]$ in 25 ml of deionized water aqueous mixed with Nickel acetate extra pure (Tetrahydrate) $(CH_3.COO)_2Ni·4H_2O$ in 25 ml of deionized water under constant stirring for 10 min. These two solutions were properly mixed together. Then the saturated solution of citric acid was added dropwise into the same mixture. After that, NH_3 was added to the precursor solution to maintain the pH of the solution as 10.3. After continuous stirring for 4 h at 70 °C, the clear solution was completely turned to a gel. Then, the gel was dried and ground into powder. The

similar procedure was followed to synthesize pure CeO_2 nanoparticles (without adding doping materials), and the product was calcined at different temperatures (200, 300, 400, 500 and 700 °C) for 2 h in a muffle furnace under an air atmosphere. Based on the TG-DTA and UV–Vis analysis of pure samples, 400 °C was selected as optimum calcination temperature. Using this temperature (400 °C), all the other different concentration of Ni-doped CeO_2 samples were prepared.

2.3. Photocatalytic activity analysis

By performing the methylene blue (MB) degradation reactions under stimulated sunlight irradiation, the photocatalytic activity of pure and Ni-doped CeO_2 nanoparticles was analyzed. 100 ml of 5×10^{-3} M aqueous MB solution and 0.2 g of fine powder catalyst were taken for this experimental work. Then suspensions were magnetically stirred for 30 min in the dark to attain adsorption-desorption equilibrium between the dye and nanoparticles. No volatility of the solvent was observed during the illumination time. Then it was continuously stirred. The aliquots of the reaction mixture were collected at regular time intervals (10 min) and centrifuged. The residual solution was analyzed using a UV-1650 PC SHIMADZU spectrometer. The period is ranging from 0 to 50 min without any adjustment of pH value (7.3). At a regular time interval, the sample aliquots were withdrawn from the reaction mixture. Changes in the concentration of MB were observed from its characteristic absorption maxima at 662 nm.

2.4. Characterization

Using SDT Q600 20 thermometer the thermogravimetric (TG) and differential thermal analysis (DTA) were carried out. The optical absorption spectra of the samples were recorded using UV-1650 PC SHIMADZU spectrometer. Using X pert PRO diffractometer with a Cu Kα radiation (Kα = 1.5406 Å), the X-ray diffraction (XRD) patterns of the products were recorded and analyzed. The morphological studies were performed on a JEOL-6610 scanning electron microscope. To know the elemental composition, Energy–dispersive X-ray analysis (EDX) was carried out using Brucker 129 eV. The HR-TEM analyses were performed on a make: FEI, model: Tecnai G2, F30. Photoluminescence measurements were done on a RF-5301 PC spectrophotometer. The FT-IR spectra were recorded (transmission mode by diluting the milled powders in KBr) by SHIMADZU-8400 Fourier-transform infrared spectrometer. The presence of functional groups in the products were analysed in the wavelength range between 4000 and 400 cm^{-1}.

3. Results and discussion

3.1. Thermal and optical properties

3.1.1. TG-DTA analysis and UV–visible

Figure 1 shows TG-DTA curves of pure CeO$_2$ particles. From DTA curve, two endothermic ($\sim$300, $\sim$500 °C) and two exothermic ($\sim$400, $\sim$700 °C) peaks are observed. TG curve shows the weight losses in all these stages. The exothermic peak appeared at $\sim$300 °C is due to condensation of cerium oxide gel particles by discharging water. The endothermic peak ($\sim$400 °C) is because of the evacuation of organic residue and the formation of crystalline CeO$_2$. The exothermic peak observed at $\sim$500 °C is due to decomposition of observed species and oxygen loss. The last endothermic peak ($\sim$700 °C) shows the event of phase changes in the cerium structure [24, 25].

In view of the progressions saw at different various temperatures from TG/DTA investigation, UV–visible spectra for the same pure CeO$_2$ particles calcined at 300, 400, 500 and 700 °C were recorded and are appeared in Fig. 2. All the spectra demonstrate the absorption maxima underneath 350 nm. The changes in the intensity of the peaks are due to change in thermal behaviour at a specific temperature. By contrasting these two investigations (TG-DTA and UV–Vis), the sample calcined at 400 °C selected. At this temperature, TG-DTA shows the formation of crystalline CeO$_2$ and UV–Vis analysis shows high blue shift which indirectly dictates its small particle size. The size of crystallites was confirmed affirmed through XRD analysis given in somewhere else. Following the above results is chosen as reasonable calcination temperature for all other Ni-doped samples and hence further studies. The UV–Vis absorption spectrum of pure and Ni-doped CeO$_2$
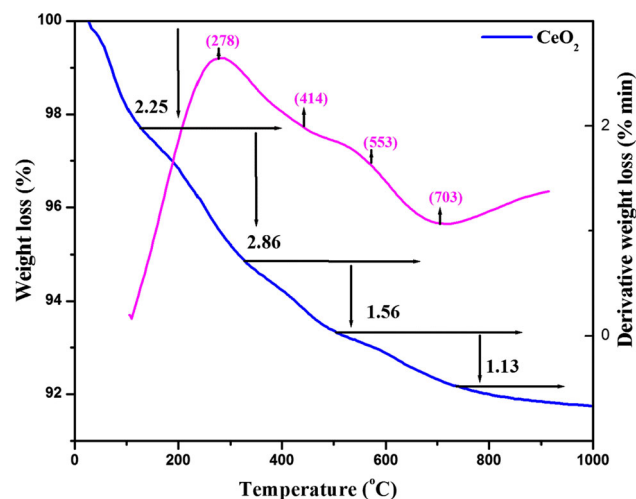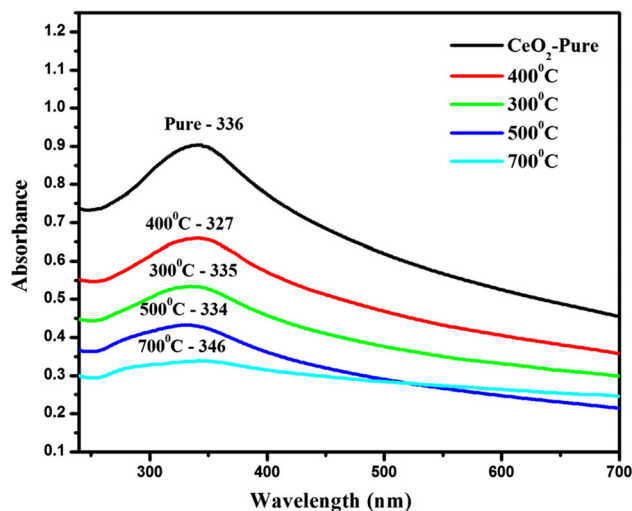
Fig. 2 UV–Vis absorption spectra for pure CeO$_2$ and calcined at different temperatures

nanoparticles calcined at 400 °C was recorded and are shown in Fig. 3. It exhibits a strong absorption band in the range 300–400 nm (Fig. 3). The fundamental absorption of the nanoparticles corresponds to electron excitation from the valence band to conduction band was computed and are utilized to determine the optical band gap by Eq. (1).

$$E_g = \frac{1240}{\lambda} \text{ eV} \tag{1}$$

where E$_g$ is the optical band gap, and λ is the absorption maximum [26, 27]. The absorption maximum for pure and Ni (0.1, 0.3, 0.5 and 0.7 M.%) doped CeO$_2$ are seen from Fig. 3.

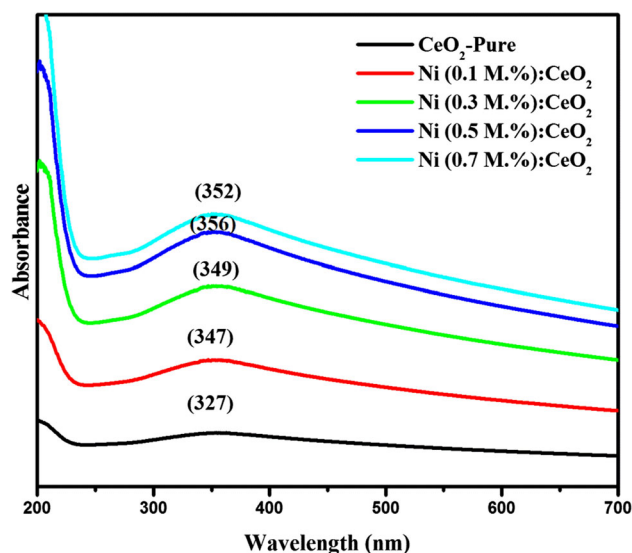**Fig. 1** Simultaneous TG-DTA curves of pure CeO$_2$ nanoparticles

Fig. 3 UV–visible absorption spectra for pure and Ni (0.1, 0.3, 0.5 and 0.7 M.%) doped CeO$_2$ nanoparticles calcined at 400 °C

The absorption coefficient α was ascertained from the absorption by the Eq. (2).

$$\alpha = \frac{2.303 \times 10^3 A\rho}{Lc} \qquad (2)$$

where A is the absorbance, ρ is the real density of CeO_2 (set at 7.28 g cm^{-3} for this calculations), L is the length of the curve and C is the concentration of the CeO_2 suspension [28]. The band gap energy corresponding to direct transition is calculated by extrapolating the linear portions of $(\alpha h\nu)^2$ as a function photon energy hν for the pure and doped nanoparticles are (Fig. 4a–e) and the values are observed at 3.79, 3. 57, 3.55, 3.48 and 3.52 eV (Table 1).

However, these values are higher than that of bulk value (3.19 eV) [29] which means a blue shift in the absorption due to quantum confinement effect. Confinement effect can affect both structural and electronic properties of nano semiconductor oxide. In the structural properties, the nanostructure may alter lattice symmetry and cell parameters. In the electronic properties, band gap and valence/conduction band/levels are disturbed [30]. The highest band gap energy value is observed for Ni (0.1 M.%) doped CeO_2 nanoparticles. The absorption of 0.5 and 0.7 M.% Ni-doped ceria experiences a red shift compared to 0.1 M.%. The redshift of an optical band gap of the ceria nanoparticles can be illustrated by two types of mechanism. The first one was due to the presence of defects caused by the charge transfer between Ce^{3+} and Ce^{4+}. This was the generally accepted mechanism for the redshift of CeO_2 nanoparticles. The second one was the size effect [31, 32]. In the present study, the redshift of the band gap indirectly dictated the increase of particle size.

3.2. X-ray diffraction study

The X-ray diffraction pattern of pure and Ni (0.1, 0.3, 0.5 and 0.7 M.%) doped CeO_2 nanoparticles were recorded and are shown in Fig. 5. The planes observed from XRD patterns are indexed for cubic structure and the lattice constant are calculated from XRD data. These are in close agreement with the JCPDS card no: 34-394 [33]. Among all the samples, 0.1 M.% of ceria shows the decrease of peak intensity with increase in FWHM which dictates its reduction of crystallite size [34].

This increase of peak broadening evidences grain refinement along with the large strain associated with the sample. Each diffraction peak of the material was rectified with the assistance of broadening due to the instrument (β_{hkl}) using the relation (3).

$$\beta_{hkl} = \left[(\beta_{hkl})^2_{measured} - (\beta_{hkl})^2_{instrumental} \right]^{1/2} \qquad (3)$$

The average nanocrystalline size is calculated using Debye– Scherrer's formula and lattice parameter are calculated by the following equation [35–37].

$$D = \frac{K\lambda}{\beta \cos \theta} \qquad (4)$$

$$a = \frac{n\lambda}{2 \sin \theta} \sqrt{h^2 + k^2} + l^2 \qquad (5)$$

where D is the crystallite size, β is the full-width of half maximum (FWHM), K is a shape factor (K = 0.9 in this work), λ is the wavelength of incident X-rays (λ = 0.15406 nm). The crystallite sizes of the pure and Ni-doped CeO_2 nanoparticles are ranged between 10.98 to 35.43 nm (Table 2). From this table, it is observed that the increase of Ni concentration increases the size of the crystallite. The minimum crystallite size was observed for 0.1 M.% of Ni-doped ceria due to quantum confinement effect.

Table 2, shows the dependence of the calculated lattice parameter (a) to the observed crystallite size of the samples. An increase in the lattice parameter was observed with a decrease in the crystallite size. As a general rule, nanoparticles of oxides exhibit a lattice expansion with a reduction in particle size while metal nanoparticles exhibit a lattice contraction. The reciprocal of the diameter (D^{-1}) is proportional to the surface to volume ratio (S/V) and consequently, the increase of the lattice parameter can be related to the higher surface to volume ratio in the smaller particles, resulting in a higher contribution from the surface layer. In oxide particles, the bond has a directional character and at the outer surface of each particle, there would be unpaired electronic orbital's, which would repel each other. This contribution from the surface layer increases with decreasing particle size and leads to larger values of the lattice parameter than in the bulk.

Generally, powder XRD is used to prove the existence of crystal structure. The XRD peak broadening is not only caused by the contribution from the crystallite domain size but also from lattice distortion caused by microstrain. The change in peak intensity and FWHM indicate the change in other lattice parameters such as microstrain, dislocation density, stacking fault and texture coefficient.

The microstrain (ε), dislocation density (δ), stacking fault (ST) and texture coefficient (TC) of pure and Ni-doped CeO_2 nanoparticles were calculated [38–41] by the following formula

$$\varepsilon = \frac{\beta \cos \theta}{4} \qquad (6)$$

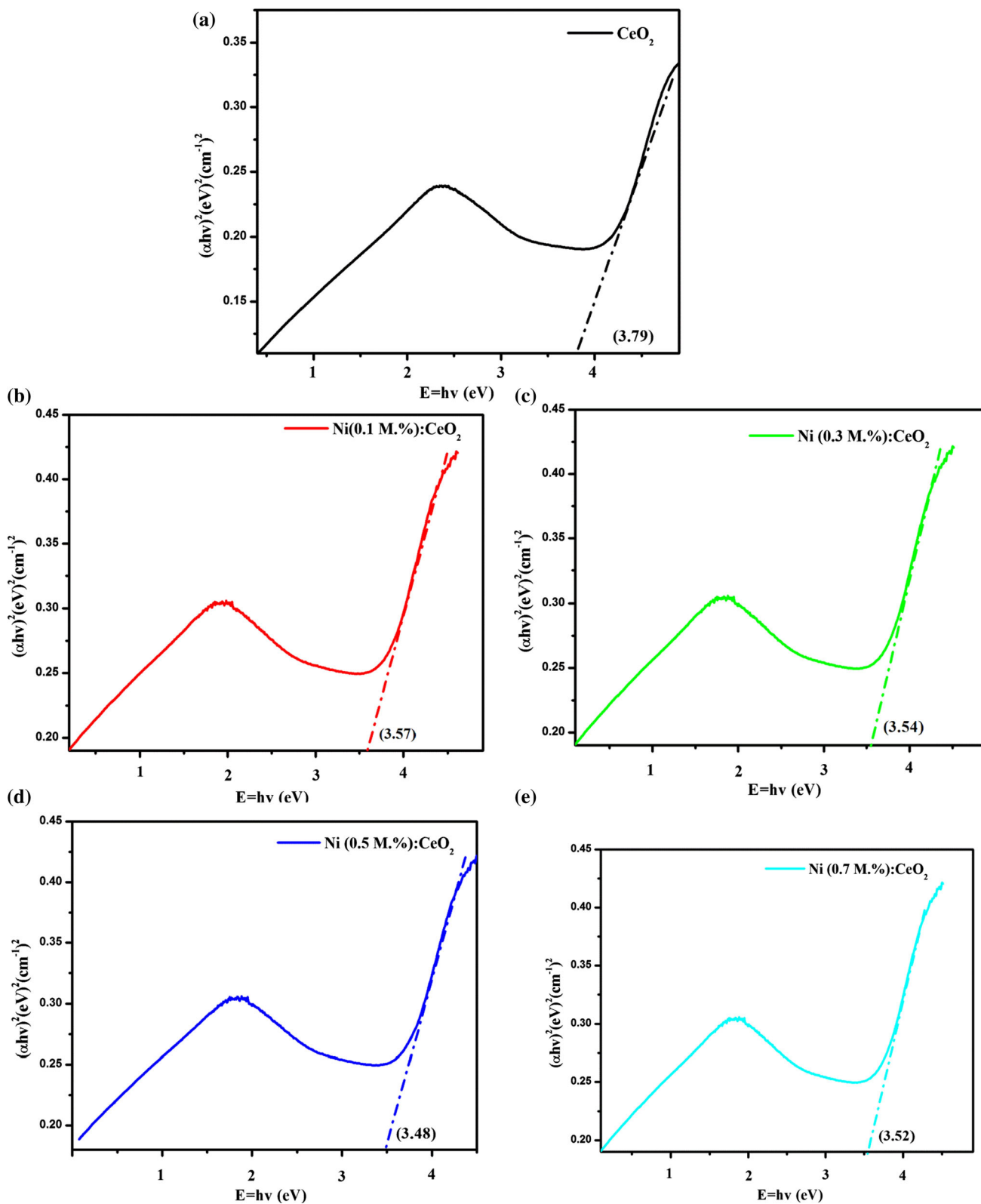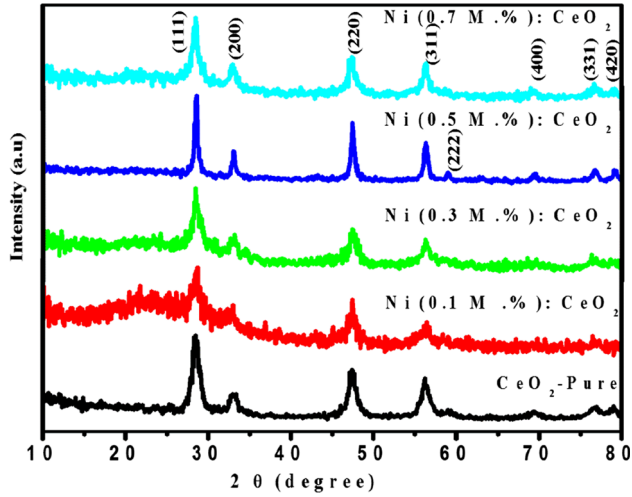$$\delta = \frac{1}{D^2} \qquad (7)$$

Fig. 4 Optical band gap graphs of pure and Ni (0.1, 0.3, 0.5 and 0.7 M.%) doped Ceria nanoparticles by Tauc plot method

Table 1 Energy band gap values of pure and Ni doped CeO_2 nanoparticles

Samples	Wavelength (nm)	From absorption band (eV)	From graph (eV)
CeO_2-Pure	327	3.79	3.79
Ni (0.1 M.%):CeO_2	347	3.57	3.57
Ni (0.3 M.%):CeO_2	349	3.55	3.55
Ni (0.5 M.%):CeO_2	356	3.48	3.48
Ni (0.7 M.%):CeO_2	352	3.52	3.52

Fig. 5 X-ray diffraction patterns of pure and Ni doped CeO_2 nanoparticles

$$SF = \left(\frac{2\pi^2}{45(tan\theta)^{1/2}} \right) \quad (8)$$

$$(Tc) = \frac{\frac{I_{(hkl)}}{I_{0(hkl)}}}{\left[Nr^{-1} \sum \frac{I_{(hkl)}}{I_{0(hkl)}} \right]} \quad (9)$$

where θ is the Bragg angle, β is the full width of half maximum (FWHM), hkl are the Miller indices, I is the intensity of the plane (111) and Nr is the number of diffraction peaks. The values are organized in Table 2. According to Theivasanthi and Alagar [42], the observation of dislocation strongly influences many of the properties of the materials. Larger the dislocation density means larger the hardness.

According to Dalpian [43] and Erwin et al. [44], the formation energy of the nanoparticles is very high, the impurity will be expelled from the cluster and incorporation should be expected just for larger nanocrystals. The decrease in dislocation density, microstrain and stacking fault improved the crystallinity of the samples [45]. According to Babitha et al. [46], the increase in microstrain and broadening of XRD peaks might occur due to the presence of oxygen (O) vacancies, structural imperfections and surface effect in ceria. This variation of microstrain arises due to lack of crystallinity as well as the small size effect. This is pictured in Fig. 6. Texture coefficient TC is used to know about the qualitative information concerning the preferential crystal orientation. If TC (hkl) $\approx$ 1 for all the (hkl) planes considered, then the nanoparticles are with a randomly oriented crystallite similar to the JCPDS reference. In the present cases, the computed values of all the

Table 2 Different parameters of pure and Ni-doped CeO_2 nanoparticles from XRD and photocatalytic activity analysis

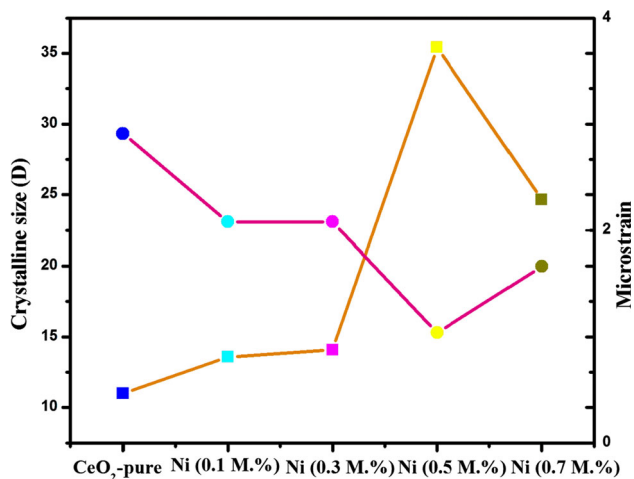| Sample name	Lattice parameter (a) nm		Dislocation density(δ) $\times 10^{16}$	Micro strain (ε) $\times 10^{-3}$	Average grain size (nm)	Photodegradation efficiency (%)
	For bulk	For nano			Scherrer's formula	
CeO_2-Pure	0.5411	0.5450	8.2945	2.9105	10.98	70
Ni (0.1 M.%):CeO_2	–	0.5429	5.4225	1.6634	13.58	80
Ni (0.3 M.%):CeO_2	–	0.5428	5.0442	2.0793	14.08	69
Ni (0.5 M.%):CeO_2	–	0.5399	7.9798	2.0785	35.43	63
Ni (0.7 M.%):CeO_2	–	0.5418	1.6524	1.0395	24.65	66

Fig. 6 Comparing to microstrain and crystallite size of pure and Ni (0.1, 0.3, 0.5 and 0.7 M.%) doped CeO$_2$ nanoparticles

planes are almost equal to 1, which implies that the nanoparticles are randomly oriented crystallite. Among the various pure and Ni-doped (0.1, 0.3, 0.5 and 0.7 M.%)

ceria, 0.1 M.% doped CeO$_2$ have lower crystalline size than others.

3.3. SEM with EDX and HR-TEM

Figure 7(a) and (b) demonstrates the SEM pictures of 0.1 M.% doped Ni ceria nanoparticles having small crystallites with aggregation. Because of smaller particles, the surface morphology is not clear. The EDX spectrum (Fig. 7c) affirmed the presence of Ce, O and Ni. The HRTEM micrograph of Ni (0.1 M.%) doped CeO$_2$ nanoparticles are recorded and are appeared in Fig. 8(a). The particle size distribution of the CeO$_2$ nanoparticles is plotted in Fig. 8(b) which indicates smaller particle size and narrow size distribution in the range 11–36 nm. The maximum number of particles are in the size of 23 nm. Each particle is a well ordered single crystal with a fringe distance of 0.35 nm (Fig. 8c). The particles were uniform in shape and also crystalline in nature as the lattice fringes could be observed from the HR-TEM image. The corresponding selected area electron diffraction (SAED) pattern
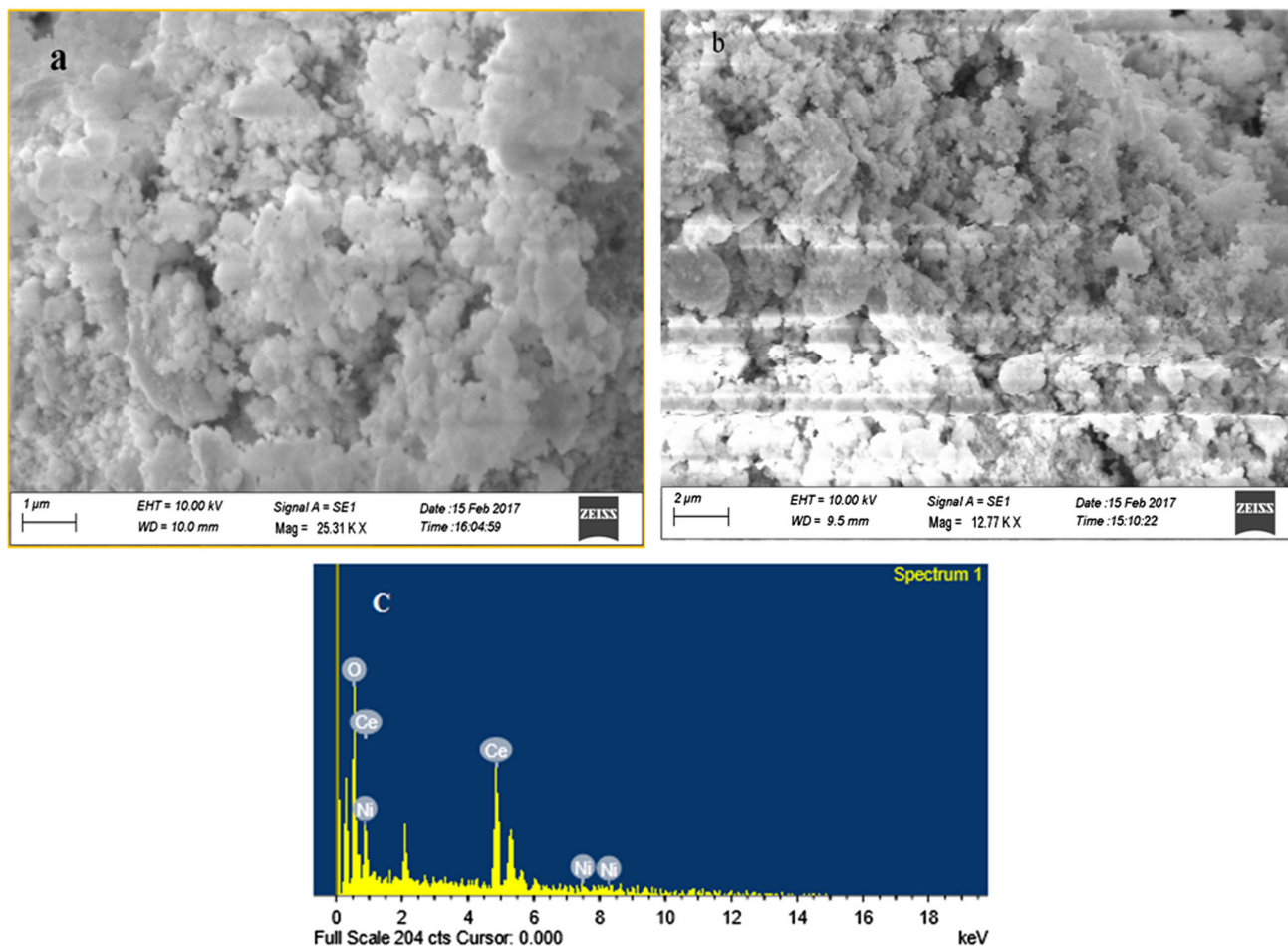

Fig. 7 SEM-EDX images (**a**) pure and (**b**) 0.1 M.% Ni doped CeO$_2$ nanoparticles (**c**) EDX spectra of Ni doped CeO$_2$ nanoparticles
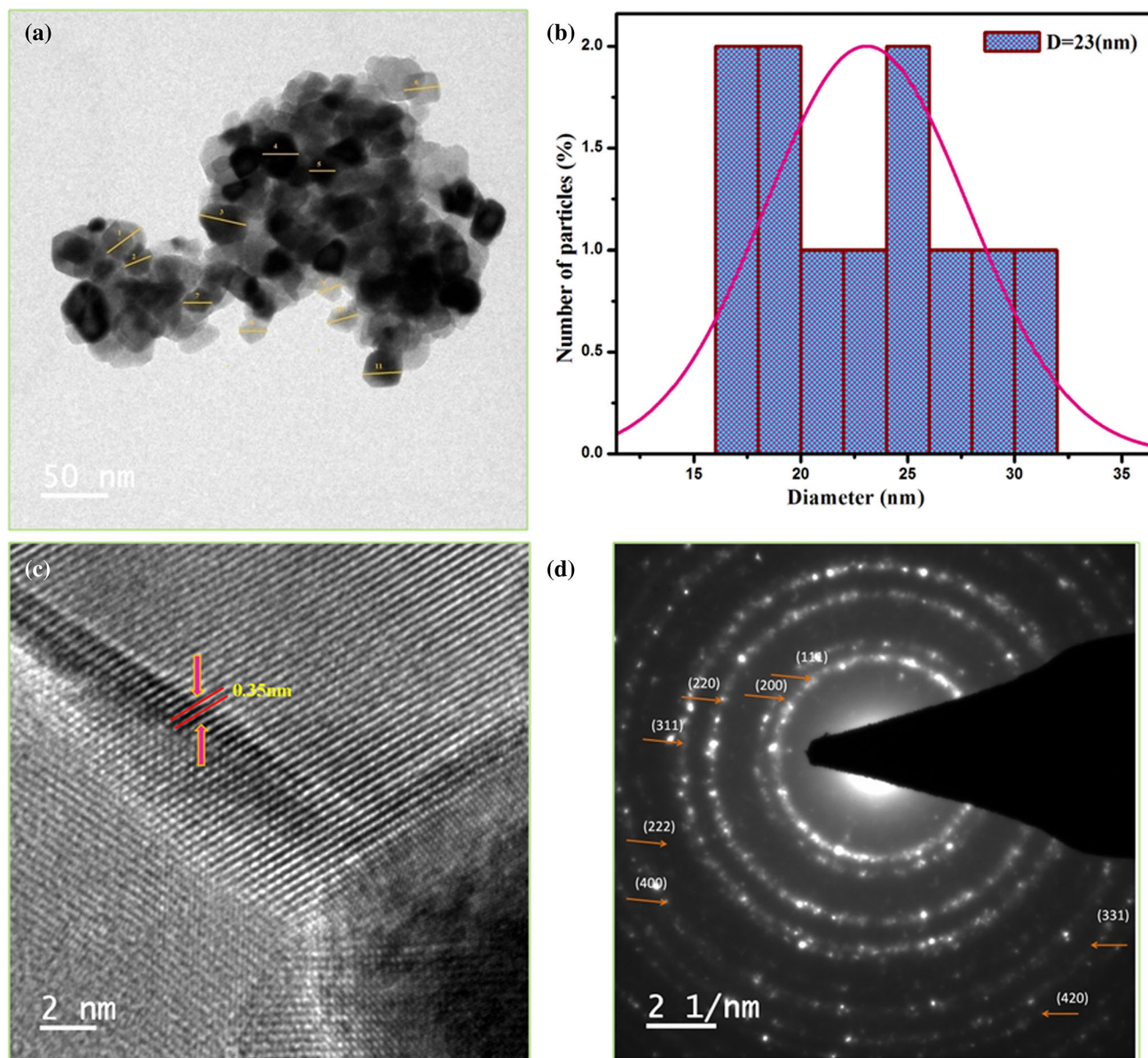
Fig. 8 (a) Particle size, HRTEM images, (b) size distribution, (c) lattice fringer and (d) SAED Pattern for 0.1 M.% Ni doped CeO_2 nanoparticles

is shown in Fig. 8(d). It displays a series of bright rings progression that they are cubic structure and is in good agreement with XRD results.

3.4. Photoluminescence (PL) spectroscopy

Figure 9 shows the PL spectra got obtained for pure and Ni (0.1, 0.3, 0.5 and 0.7 M.%) doped CeO_2 nanoparticles utilizing the excitation wavelength of 352 nm. The PL spectrum can reveal important information about the surface defect, oxygen vacancies and surface states, which can strongly affect the photocatalytic reactions [47]. Figure 9 demonstrates the intensity of PL emission changes with oxygen ions. The increase of Ni content is associated with

structural disorganization level, and the charge transfer occurring between cerium, Ni and oxygen ions. The increase of Ni content significantly raises the particle size up to 0.5 M.% which allows faster recombination of electrons in Ce 4f and Ni 3d conduction bands with holes in O 2p valence band by increasing PL signal [48]. Moreover, each spectrum contains different emission bands. The two blue emission bands at 420 (2.95 eV) and 457 nm (2.71 eV) are related to the abundant defect such as dislocations, which is helpful for fast oxygen transportation Ce 4f level with a width of 1 eV is localized at the forbidden gap. This lies at 3 eV over the valence band (O 2p). A weak blue-green emission located at 481 nm (2.57 eV) is possibly due to surface defects in the Ni-doped CeO_2
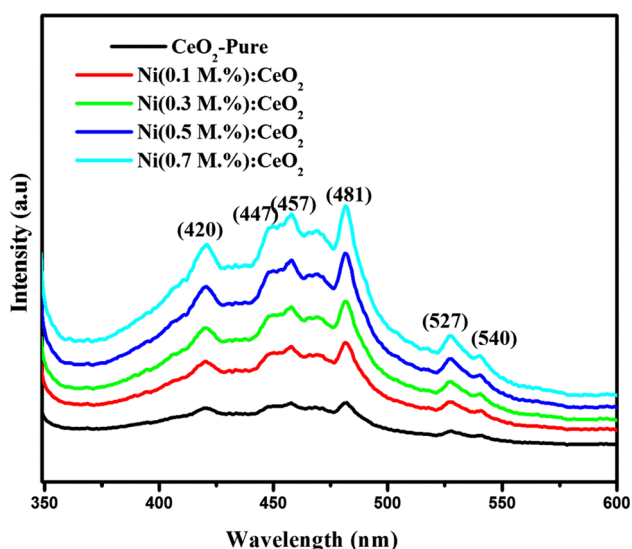
Fig. 9 Photoluminescence spectra of pure and Ni (0.1, 0.3, 0.5 and 0.7 M.%) doped CeO$_2$ nanoparticles
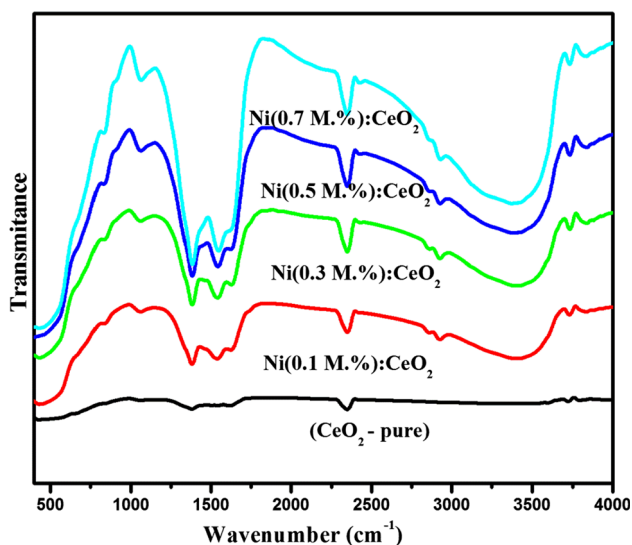

Fig. 10 FTIR spectra of pure and Ni (0.1, 0.3, 0.5 and 0.7 M.%) doped CeO$_2$ nanoparticles

nanoparticles [49]. The low intensity of the green emission band at 527 nm (2.35 eV) may be due to the low density of oxygen vacancies generated during the preparation of the CeO$_2$ samples [50]. It can be seen that PL emission bands of doped samples are red shifted (Fig. 9) compared to pure CeO$_2$. The broad PL band ranging from 350 to 600 nm of all the samples could be the result of defects including oxygen vacancies in the crystal with electronic energy levels below the 4f band.

3.5. Fourier transforms infrared spectroscopy (FTIR)

FT-IR transmittance spectra of as-synthesized pure and different concentration of Ni-doped CeO$_2$ nanoparticles were recorded in the wave number range of 4000–400 cm^{-1} and are appeared in Fig. 10. The intense absorption band at 3419 cm^{-1} corresponds to the O-H mode of (H-bonded) water molecules. There are peaks at 2920 and 2850 cm^{-1}, corresponding to the asymmetric and symmetric stretching vibrations of C-CH$_2$ in the methylene chains. A peak at 1634 cm^{-1} is specified as the deformation of –CH$_2$ and –CH$_3$ symmetric stretching vibrations of the surfactant [51]. In the FTIR spectrum, the peak at 1543 cm^{-1} belongs to carboxylate vibration (CO$_2$) stretching [52]. It is also seen that the absorption band at 833 cm^{-1} produced by CeO$_2$, is because of Ce–O stretching vibrations [53].

3.6. Photocatalytic activity

Figure 11(a–e) demonstrates the level of highest photocatalytic activity of pure and different concentration of Ni-doped CeO$_2$ nanoparticles. The degradation behaviour was studied at an interim of 10 min up to 50 min. Increasing of time increases the % of degradation. The maximum degradation is obtained after 50 min.

The percentage of photodegradation efficiency of the materials is determined using the following expression (Table 2).

$$\%D = \frac{C0 - C}{C0} \times 100 \qquad (10)$$

where C_0 is the initial concentration of MB and C is the remaining concentration of MB after irradiation in the desired time interval [54].

Figure 12(a) shows the degradation curve for pure and Ni-doped CeO$_2$ nanoparticles under stimulated sunlight irradiation. It was observed from the detailed photocatalytic experiments that the absorbance of dye solution decreases with increasing the illumination time. After Ni doping, high degradation efficiency (80%) was observed in 50 min for the lowest concentration (0.1 M.%). Moreover, increasing of dopant concentration shows a decrease in degradation up to 0.5 M.%. According to Huang et al. [55], the distinction of photocatalytic performance is mainly sourced from the different amount of oxygen vacancies. The separation of electron-hole pairs is related to the number of oxygen vacancies present. They also suggested that, much more oxygen vacancies would allow fast electron-hole recombination, thereby decreasing the photocatalytic activity. However, further increase of dopant concentration (0.7 M.%) increases the degradation once again.
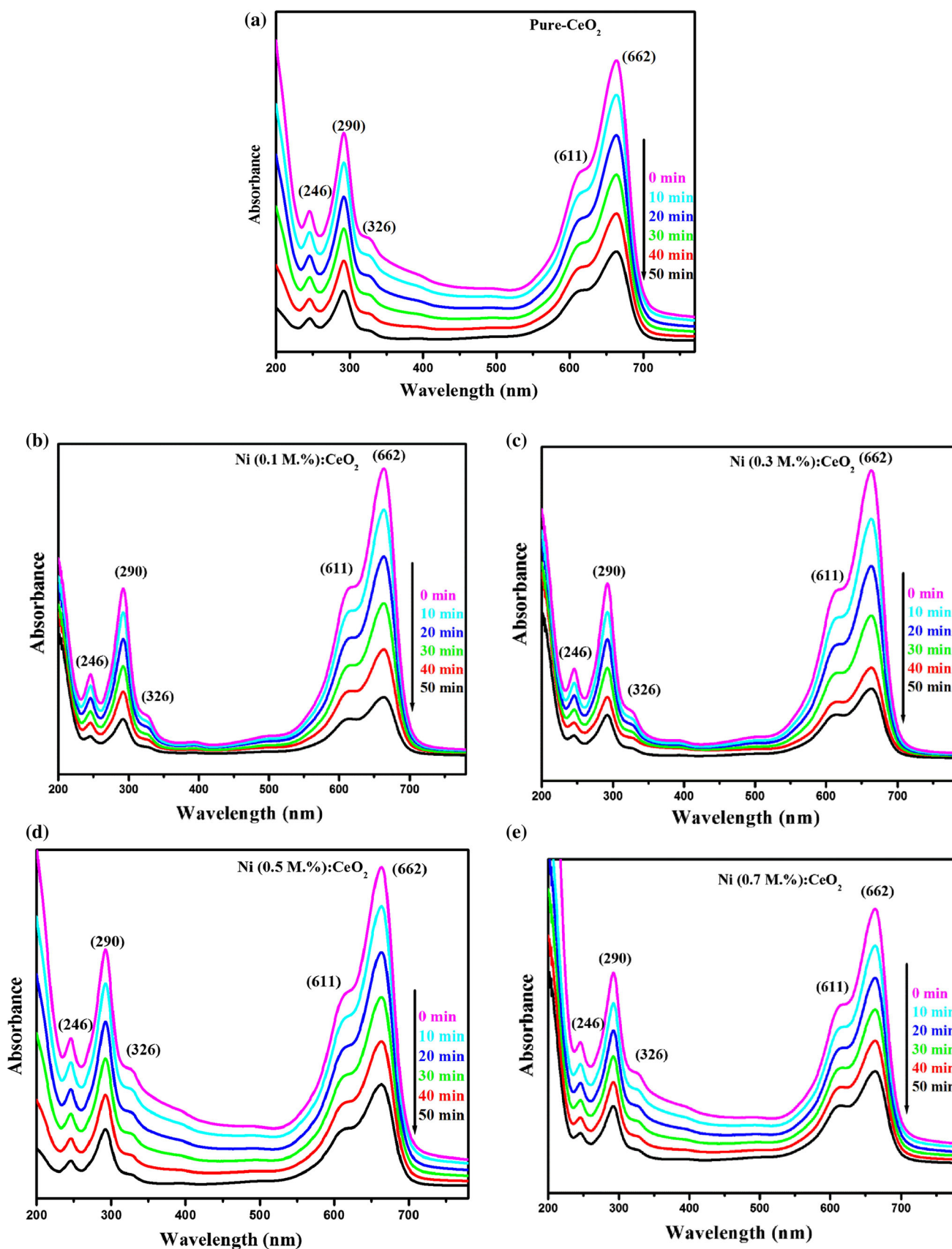
Fig. 11 (**a–e**) Photocatalytic activity of UV–Vis absorbance spectra of (**a**) pure and (**b–e**) Ni (0.1, 0.3, 0.5 and 0.7 M.%) doped CeO$_2$ nanoparticles
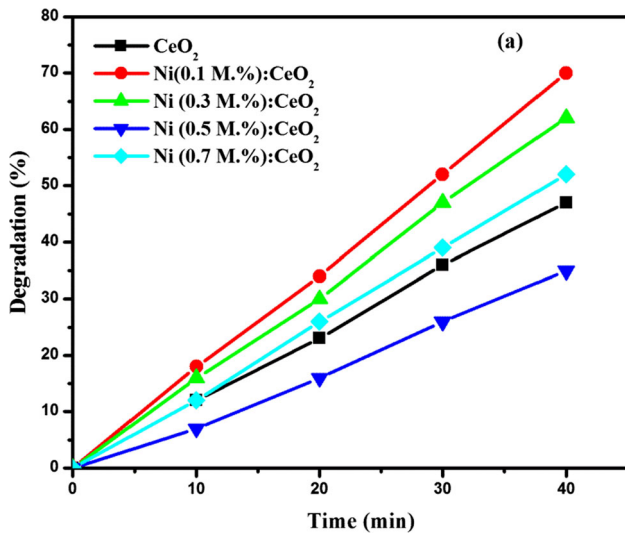
Fig. 12 Time period percentage degradation efficiency of pure and Ni (0.1, 0.3, 0.5 and 0.7 M.%) doped CeO₂ nanoparticles

According to Malleshappa et al. [56], the differences in photocatalytic activity were highly related to the concentration defects on the surface of the nanoparticles. They also stated that, the particle size decreases, surface defects increases and hence the charge carrier recombination rate increases which results in the increased photocatalytic activity. In the present study, 0.1 M.% of Ni-doped CeO₂ having smallest particle sizes show high photocatalytic activity, which was attributed to the high abilities of separations photogenerated charge carriers, large specific surface area and enhanced light absorption.

Figure 13 shows the mechanism of photocatalysis. When the electron in the valence band of the semiconductor absorbs a photon with energy greater than the band gap of the semiconductor, the electron becomes excited and jumps to the conduction band, leaving a positively charged hole in the valence band. Besides recombination with the electron, the positively charged hole can oxidize water molecules to form hyper-reactive hydroxyl free radicals (˙OH). The resulting hydroxyl radicals are the main agents that attack the chemical pollutant molecules to purify water. The excited electron can react with a dissolved oxygen molecule to form oxygen radical, which is also active toward organic pollutants.

Thus it is observed that the electrons play a predominance role in the progress of photodegradation of MB organic pollutants. According to Li et al. [57] and Xu et al. [58], the electrons trapped by Ce 4f orbitals decrease the photocatalytic activity. It has been observed that the degradation of the compound proceeds much more rapidly in the presence of Ni/CeO₂ doped catalyst in stimulated sunlight. The reason for better photoactivity could be attributed to the fact that the catalyst is composed of nano size and nanocrystalline form.

4. Conclusions

Utilizing sol–gel method, the pure and different concentration of Ni-doped CeO₂ nanoparticles have been successfully synthesized. The effect of particle size on structural parameters such as lattice parameter (α), dislocation density (δ), microstrain (ε) have been noticed from XRD analysis. The XRD patterns also showed that the materials were in nanometer regime (10.98–35.43 nm) with cubic structure. The blue shift of 0.1 M.% Ni: CeO₂ from high concentration samples is due to quantum confinement effect. The band gap energy of pure CeO₂ nanoparticles observed by UV–visible is greater than that

Fig. 13 Photocatalytic mechanism
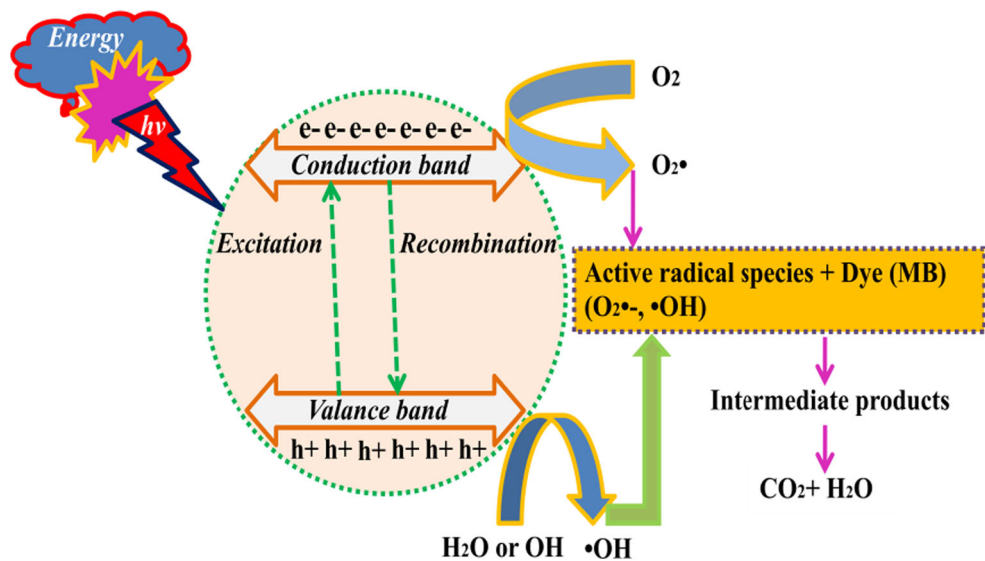
of reported bulk values. The blue-green emission band at 481 nm was observed due to the presence of oxygen vacancy and oxygen interstitial defects. The various bond vibrational modes are assigned for both doped and pure ceria with the help of FTIR spectral analysis. The high performance of photocatalytic activity was found to 50 min irradiation time for 0.1 M.% Ni-doped CeO_2 nanoparticles. Along these line it is inferred that the synthesized Ni/CeO_2 is one of the best candidates for environmental applications as a photocatalyst, which was ascribed to the large specific surface area, high ability of separations photo-generated charge carries and the improve light absorption.

References

[1] X Wang, P Wu, Z Huang, N Zhu, J Wu, P Li and Z Dang *Appl. Clay. Sci.* **95** 95 (2014)

[2] X Yan, T Ohno, K Nishijima, R Abe and B Ohtani *Phys. Lett.* **429** 606 (2006)

[3] E A El-Sharkawy, A Y Soliman and K M Al-Amer *Adv. Colloid. Interface. Sci.* **310** 498 (2007)

[4] S Vadivel, M Vanitha, A Muthukrishnaraj and N Balasubramanian *J Water Process Eng.* **1** 17 (2014)

[5] K L Ameta, N Papnai and R Ameta *J. Mater.* 1 (2014)

[6] Y Huang, H Xu, H Yang, Y Lin, H Liu, and Y Tong *ACS Sust. Chem. Eng.* **6** 2751–2757 (2018)

[7] Z Hu, S Haneklaus, G Sparovek and E Schnug *Commun. Soil. Sci. Plant. Anal.* **37** 1381 (2006)

[8] A Medalia and B Byrne *Anal. Chim.* **23** 453 (1951)

[9] M. Darroudi, M Hakimi, M Sarani, R Kazemi-Oskuee, A Khorsand-Zak and L Gholami *Ceram. Int.* **39** 6917 (2013)

[10] R B Duarte, M Nachtegaal, JMC Bueno and JA Van Bokhoven *J. Catal.* **296** 86 (2012)

[11] V B Mortola, S Damyanova, D Zanchet and J M C Bueno *Appl. Catal. B: Environ.* **107** 221 (2011)

[12] G Montes-Hernandez, R Chiriac, N Findling, F Toche and F Renard *Mater. Chem. Phys.* **172** 202 (2016)

[13] A B Stambouli and E Traversa *Sustain. Energy. Rev.* **6** 433 (2002)

[14] E Bekyarova, P Fornasiero, J Kašpar and M Graziani *Catal. Today.* **45** 179 (1998)

[15] S Yabe, J. Solid *State. Chem.* **17** 17 (2003)

[16] S B Khan, M Faisal, M M Rahman and A Jamal *Total Environ.* **409** 2987 (2011)

[17] S D Senanayake, D Stacchiola and J A Rodriguez *Acc. Chem. Res.* **46** 1702 (2013)

[18] H I Chen *Ceram. Int.* **31** 795 (2005)

[19] H W He, X Q Wu, W Ren, P Shi, X Yao and Z T Song *Ceram. Int.* **38** S501 (2012)

[20] V Sharma, K M Eberhardt, R Sharma, J B Adams, P A Crozier *Chem. Phys. Lett.* **495** 280 (2010)

[21] M A Gabal, S A K Elroby and A Y Obaid *Powder. Technol.* **229** 112 (2012)

[22] K Nagy and I Dékány *Colloids. Surf. A Physicochem. Eng. Asp.* **345** 31 (2009)

[23] L Guerbous and A Boukerika *J. Nanomater.* 1 (2015)

[24] K Gopinath, V Karthika, C Sundaravadivelan and S Gowri *J. Nanostruct. Chem.* **5** 295 (2015)

[25] S Gnanam and V Rajendran *J. Sol-Gel. Sci. Technol.* **58** 62 (2010)

[26] E D Sherly, J J Vijaya and L J Kennedy *J. Mol. Struct.* **1099** 114 (2015)

[27] M Darroudi, S J Hoseini, R Kazemi Oskuee, H A Hosseini, L Gholami and S Gerayli *Ceram. Int.* **40** 7425 (2014)

[28] F Cheviré, F Muñoz, C F Baker, F Tessier, O Larcher, S Boujday, C Colbeau-Justin and R Marchand *J. Solid. State. Chem.* **179** 3184 (2006)

[29] S Samiee and E K Goharshadi *Mater. Res. Bull.* **47** 1089 (2012)

[30] M D Hernandez-Alonso, A B Hungria, A Martinez-Arias, J M Coronado, J C Conesa, J Soria and M Fernandez-Garcia *Phys. Chem. Chem. Phy.* **6** 3524 (2004)

[31] H I Chen and H Y Chang *Solid. State. Commun.* **133** 593 (2005)

[32] X H Lu, X Huang, S L Xie, D Z Zheng, Z Q Liu, C L Liang and Y X Tong *Langmuir.* **26** 7569 (2010)

[33] J Zhang, H Yang, S Wang, W Liu, X Liu, J Guo and Y Yang *Cryst. Eng. Comm.* **16** 8777 (2014)

[34] X Yang, X Yu and G Li *J. Mater. Sci Mater. El.* **27** 9704 (2016)

[35] P Scherrer, Gottinger *Nachrichten.* **2** p 98 (1918)

[36] S Mishra, S H Sonawane, N Badgujar, K Gurav and D Patil *J. Appl. Polym. Sci.* **96** (2005)

[37] R Suresh, V Ponnuswamy and R Mariappan *Mater. Tech.* **30** 12 (2014)

[38] E M Nasir *Res. Sci. Eng. Tech.* **3** 2319 (2014)

[39] G K Williamson and R E Smallman *Philos. Mag.* **1** 34 (1956)

[40] M M Vora and A M Vora *J. Electron Devices.* **12** 734 (2012)

[41] V Ramasamy and G Vijayalakshmi *J. Mater. Sci. Mater. El.* **27** 5 (2016)

[42] T Theivasanthi, A M Konjac *Nano. Biomed. Eng.* **5** 1 (2013)

[43] G M Dalpian, J R Chelikowsky *J. Phys. Rev. Lett.* **96** 22 (2006)

[44] S C Erwin, L Zu, M I Haftel, A L Efros, A Kennedy and D J Norris *Nature (London)* **436** 91 (2005)

[45] R Suresh, V Ponnuswamy and R Mariappan *Appl. Surf. Sci.* **273** 457 (2013)

[46] K K Babitha, K P Priyanka, A Sreedevi, S Ganesh and T Varghese *Mater. Charact.* **98** 222 (2014)

[47] E D Sherly, J Judith Vijaya and L John Kennedy *J. Mol. Struct.* 1099 (2015)

[48] R C Deus, J A Cortes, M A Ramirez, M A Ponce, J Andres, L S R Rocha, E Longo and A Z Simões *Mater. Res. Bull.* **70** 416 (2015)

[49] C L Chai, S Y Yang, Z K Liu, M Y Liao and N F Chen *Sci. Bull.* **48** 1198 (2003)

[50] S Maensiri, S Labuayai, P Laokul, J Klinkaewnarong and E Swatsitang *J. Appl. Phys.* **53** 06J (2014)

[51] N Krishna Chandar and R Jayavel *Physica. E* **58** 48 (2014)

[52] H Gu and M D Soucek *Chem. Mater.* **19** 1103 (2007)

[53] K K Babitha, A Sreedevi, K P Priyanka, B Sabu and T Varghese *Indian. J. Pure. Appl. Phys.* **53** 596 (2015)

[54] A B Sifontes, M Rosales, F J Méndez, O Oviedo and T Zoltan *J. Nanomater.* 1 (2013)

[55] Y Huang, B Long, M Tang, Z Rui, M Sadeeq Balogun, Y Tong and H Ji *Appl. Catal B. Environ.* **181** 779–787 (2016)

[56] J Malleshappa, H Nagabhushana, S C Sharma, Y S Vidya, K S Anantharaju, S C Prashantha, B Daruka Prasad, H Raja Naika, K Lingaraju and B S Surendra *Acta. Mol. Biomol. Spectrosc.* **149** 452 (2015)

[57] Q Li, S Mahendra, D Y Lyon, L Brunet, M V Liga, D Li and P J J Alvarez *Water. Res.* **42** 4591 (2008)

[58] C Xu, G P Rangaiah and X S Zhao *Ind. Eng. Chem. Res.* **53** 14641 (2014)